

# Effect of Al content on the oxidation behavior of NiCoCrAlYHf alloys at 1100

**DOI:**
10.1016/j.corsci.2023.111417

**Document Version**
Accepted author manuscript

# Effect of Al content on the oxidation behavior of NiCoCrAlYHf alloys at 1100°C

Aihui Huang [a], Ying Chen [b, c], Zhao Zhang [d], Jianyu Shen [e], Ling Li [a], Xuanzhen Liu [a], Han Zhang [a], Jie Lu [a,*], Xiaofeng Zhao [a,*]

[a] Shanghai Key Laboratory of Advanced High-Temperature Materials and Precision Forming, School of Materials Science and Engineering, Shanghai Jiao Tong University, Shanghai, 200240, China

[b] Department of Materials, The University of Manchester, Manchester M13 9PL, United Kingdom

[c] The Henry Royce Institute, The University of Manchester, Manchester M13 9PL, United Kingdom

[d] State Key Laboratory of Metal Matrix Composites, School of Materials Science and Engineering, Shanghai Jiao Tong University, Shanghai 200240, China.

[e] GRINM Resources and Environment Tech. Co. Ltd., Beijing100088, China.

**Abstract:**

The effect of Al content on the oxidation behavior of NiCoCrAlYHf alloys (Ni44Al16, Ni42Al18 and Ni40Al20) at 1100°C is investigated in this study. It is demonstrated that the oxidation rate of NiCoCrAlYHf alloy decreases with the increase of Al content. The Al content play the important role on the oxidation rate by determining the columnar grain size of α-$Al_2O_3$ scale and the distribution of Y/Hf-rich oxides within the α-$Al_2O_3$ scale, which shows large influence on O diffusion rate. Those findings can provide guidance for the high-performance NiCoCrAlYHf coatings design.

Keywords: Al content; Oxidation behavior; NiCoCrAlYHf alloy.

* Corresponding authors: Jie Lu (lu-jie@sjtu.edu.cn); Xiaofeng Zhao (xiaofengzhao@sjtu.edu.cn)

## 1.Introduction

NiCoCrAlY alloys are widely used as bond coat materials for thermal barrier coatings or protective coatings for aeroengines and gas turbines owing to their excellent oxidation resistance at elevated temperature [1-4], which can be traced back to the efforts made in optimizing the oxidation resistance of NiCrAl alloys since the 1970s [5-7]. However, the use of conventional NiCoCrAlY alloys is limited to 1100℃ due to accelerated oxidation above this temperature, which increases the elastic strain energy stored in oxide scales. Once the elastic strain energy exceeds the fracture toughness at the scale/alloy interface, spallation and failure of oxide scales will occur [8]. Therefore, lowering the oxidation rates of NiCoCrAlY alloys is essential to improving their temperature capability and extending their lifetime [9-10].

Several approaches have been developed to reduce the oxidation rates of NiCoCrAlY alloys [11-16]. Grain refinement can suppress the formation of non-protective oxides (e.g. spinel) by reducing the threshold of Al concentration to form an exclusive $Al_2O_3$ scale, which will effectively reduce the oxidation growth rate at early stage of oxidation [11-12]. Nevertheless, this method has limited influence on the thickening rate of oxide scale during prolonged oxidation. Alloying platinum is another effective method to promote selective oxidation of Al and improve resistance to oxide spallation [13-14]. However, the high cost of Pt limits its applications to high-value components of aeroengines (e.g. turbine blades). Homogenizing the distribution of reactive elements (RE) through powder milling is also an effective method to decrease the oxidation rate of NiCoCrAlY alloys by strengthening the RE effect [15-16]. However, the milling process involved in this method is detrimental to powder flowability required for thermal spray and increase the processing cost. Therefore, it is important to develop a simple, low-cost and effective method to lower the oxidation rates of NiCoCrAlY alloys. Tunning the composition of NiCoCrAlY alloy may be economical and feasible method to decrease the oxidation rate of NiCoCrAlY alloy. This method does not need the precious metal elements and other preparation process.

It is well accepted that the growth of $Al_2O_3$ was determined by concurrent Al and O

ions diffusion along the $Al_2O_3$ grain boundaries at high temperatures [17-18]. However, when the base alloys are doped with minor reactive elements (REs) such as Y, Zr and Hf, the growth of $Al_2O_3$ is dominated by inward O diffusion [19-20]. The distribution and content of REs have critical effect on the O diffusion rate, as the REs-rich oxides can be the short-circuit path for O diffusion [21]. Meanwhile, the microstructure of NiCoCrAl determined by the composition have important influence on the distribution and solubility of REs [22]. The composition of NiCoCrAlY alloy also play an important role on the Al activity and Al diffusivity [23-24]. Unfortunately, little work has done for the effect of microstructural variation on the oxidation behavior of NiCoCrAl alloy, especially for the Al diffusion and O diffusion. Therefore, the Al content is chosen for studying the effect of microstructural variation. On the one hand, the Al content is crucial for the microstructure and Al diffusivity of NiCoCrAl alloy [25-27]. Besides, the Ni content is regarded as the balanced content along with the Al content changes due to the lower formation enthalpy of Ni-Al than Cr-Al and Co-Al [28], which will have important influence on the phase constitutions of NiCoCrAl alloy.

In this study, the effect of Al content on oxidation behavior of YHf co-doped $Ni_{60-x}Co_{20}Cr_{20}Al_x$ (x=16, 18 and 20 at.%) alloys at 1100℃ was investigated by a combination of thermodynamic calculations and experiments. REs (Y/Hf) were added into the alloys for improving their oxidation resistance due to their proven beneficial effect in the scale adhesion [29-31]. Our findings provide scientific guidance for compositional design of NiCoCrAlYHf coatings to further improve their oxidation resistance.

## 2. Materials and methods

### *2.1 Compositional design*

To guide the design of NiCoCrAl alloys with varying Al content, the pseudo-quaternary phase diagram of the $Ni_{60-x}Co_{20}Cr_{20}Al_x$ system (**Fig. 1a**) was calculated by the CALPHAD approach using the Phase-diagram module of Thermo-calc (TC) software and thermodynamic database (TCNI8) [32-33]. The Cr and Co contents were fixed at 20 at.% to achieve good hot corrosion resistance [34-35]. The minor reactive elements Y and Hf were not included in the calculation due to their low concentrations (Y:0.025 at%, Hf: ~0.025 at%). Conventional NiCoCrAlY alloy usually has two phases: the NiAl-based β phase and the Ni-based γ phase. The β phase provides the sufficient Al element to develop $Al_2O_3$ scale, while the γ phase offered the mechanical properties for reducing the possibility of brittle cracking during the thermo-mechanical process. Therefore, the enlarged γ+β zone is shown in **Fig. 1b** to maintain the consistency with microstructure (γ+β phase) of conventional NiCoCrAlY alloy. Three compositions, $Ni_{44}Co_{20}Cr_{20}Al_{16}$ (Ni44Al16), $Ni_{42}Co_{20}Cr_{20}Al_{18}$ (Ni42Al18), $Ni_{40}Co_{20}Cr_{20}Al_{20}$ (Ni40Al20), were selected for our research. The minimum Al content is set as 16 at.% to guarantee sufficient Al supply for formation of $Al_2O_3$ scales [36]. Considering the ductility of NiCoCrAlYHf alloy, the maximum Al content is set as 20 at.%. The phase fractions of the three alloy compositions were also calculated using TC and shown in **Fig. 1c-e**. It can be seen that all the alloys possess a mixture of γ and β phase at 1100℃. To build the relationship between the Al content and high temperature oxidation behavior of those alloys, the Al diffusion coefficient of those alloys at 1100℃ was also calculated by the TC, assisted by the DICTRA module and MOBNI4 kinetic database. The Y/Hf solubility of each alloy was also calculated by ONE AXIS EQUILIBRIUM module of TC to study the distribution of Y/Hf-rich precipitates.

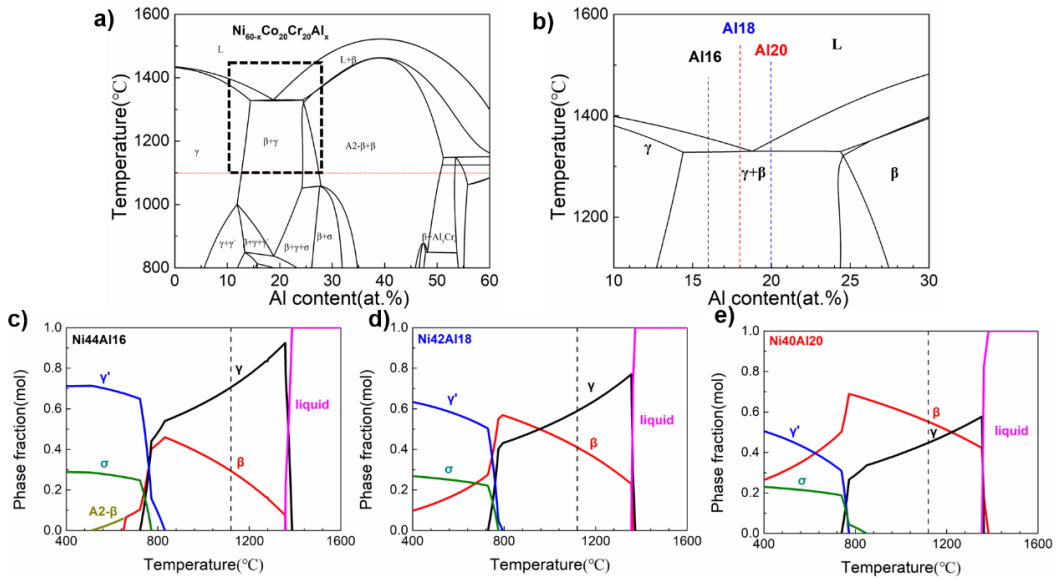


Fig. 1 Thermodynamic calculations of the $Ni_{60-x}Co_{20}Cr_{20}Al_x$ system: a) the pseudo-quaternary phase diagram; b) the enlarged view of the black frame in a). The three alloy compositions are marked on the diagram. c-e) the phase fractions of Ni44Al16, Ni42Al18 and Ni40Al20 alloys, respectively, as a function of temperature (A2-β means disordered BCC crystal structure). The black dash lines represent the oxidation temperature (1100°C) used in this work.

### *2.2 Materials preparation*

Three $Ni_{60-x}Co_{20}Cr_{20}Al_x$ (x=16, 18 and 20, respectively, in at.%) alloys were manufactured using arc-melting in a titanium-getter argon atmosphere with high purity element constituents (purity >99.9 wt%). Reactive elements Y and Hf (purity > 99.9 wt.%) with a doping concentration of 0.025 at.% were added into three alloys to enhance the oxide scale adhesion (Y) and reduce the oxidation growth rate (Hf) [37]. The as-cast ingots were remelted at least five times to achieve microstructural homogeneity in the alloys.

### *2.3 Isothermal oxidation test*

Rectangular plates with a dimension of 10 × 10 × 2.5 $mm^3$ were cut from the as-cast ingots using a precision cut-off machine. The samples were mechanically ground to a mirror finish using a 5000 SiC grit paper and ultrasonically cleaned in acetone for 5 minutes. Isothermal oxidation test was carried out at 1100 °C in a chamber furnace in

laboratory air for up to 500 h. After required exposure time, samples were removed from the furnace and air-cooled for 10 min using a fan outside of the furnace.

*2.4 Samples characterization*

The phase structures of the alloys were identified using X-ray diffraction (XRD,Bruker D8 ADVANCE). The microstructures and compositions of the alloys and oxides were studied by a scanning electron microscope (SEM, Mira3, Tescan) fitted with energy dispersive X-ray spectroscopy (EDS, Oxford Instruments) and electron backscatter diffraction (EBSD, Oxford Instruments NordlysMax3). The analytical scanning transmission electron microscope (STEM, Talos F200X G2, Thermo Fisher Scientific, USA) combined with energy-dispersive X-ray spectroscopy (EDS) system was used to identify the chemical composition of oxidation scale. The microscope was operated at 200 kV. The TEM lamella was prepared using the focused ion beam (FIB, GAIA3, Tescan, Czech Republic). To identify the phase transformation of the grown $Al_2O_3$ in the early oxidation stage, Photoluminescence piezospectroscopy (PLPS) was employed for testing by using a confocal Raman microprobe (LabRAM HR, Horiba Jobin Yvon,France) fitted with a 532 nm Nd:YAG laser. The spectra were fitted using mixed Gaussian-Lorentzian functions (Labspec software) to obtain the peak positions.

## 3. Results

### *3.1 Microstructures of YHf co-doped $Ni_{60-x}Co_{20}Cr_{20}Al_x$ alloys*

The XRD results in **Fig. 2** show that the three alloys are double-phase structure composed of γ and β phase, which are well in agreement with the calculated results in **Fig. 1c-e**. **Fig. 3** shows the microstructural analysis of the three alloys. According to the BSE images and EBSD phase maps, all alloys consist of a continuous γ matrix (bright contrast in **Fig. 3a-c**) and numerous β-precipitates (dark contrast in **Fig. 3a-c**). Based on the SEM-EDS point analysis (**Table. 2**), the γ phase is enriched with CoCr but the β phase is enriched with NiAl. As the Al content increases from 16 at.% to 20 at.%, the volume faction of γ phase decreases from 81.6±1.5% to 34.5±2.5% but the volume faction of β phase increases from 17.4±1.6% to 65.2±2.3% (**Table. 1**). Moreover, the amount and size of Y/Hf precipitates decrease along with the increase of Al content (see the white contrast and black arrow in the **Fig. 3a-c**).

Table 1 Volume fractions of γ phase and β phase in three alloys. (The volume fraction is the average value taken from five EBSD maps with a magnification of 500X)

| Alloy | γ phase fraction | β phase fraction |
|---|---|---|
| Ni44 Al16 | 81.6±1.5% | 17.3±1.6% |
| Ni42 Al18 | 68.5±2.1% | 31±1.7% |
| Ni40 Al20 | 34.5±2.5% | 65.2±2.3% |

Table 2 Chemical compositions (at.%) of β and γ in each alloy (The chemical composition is the average value taken from EDS analysis in five different points).

| Elements | Ni44Al16 | | Ni42Al18 | | Ni40Al20 | |
|---|---|---|---|---|---|---|
| | β | γ | β | γ | β | γ |
| Ni | 46.8±1.6 | 42.1±1.4 | 43.3±2.5 | 36.4±1.9 | 40.4±1.7 | 37.4±1.8 |
| Co | 14.5±1.7 | 21.9±1.6 | 13.8±1.6 | 24.7±1.4 | 16.3±1.5 | 24.2±2.5 |
| Cr | 8.5±1.5 | 23.2±2.3 | 10.5±2.5 | 27.2±1.2 | 15.4±2.7 | 25.5±1.4 |
| Al | 33.2±2.2 | 12.8±1.2 | 32.4±1.7 | 11.7±1.6 | 27.9±1.4 | 12.9±1.9 |

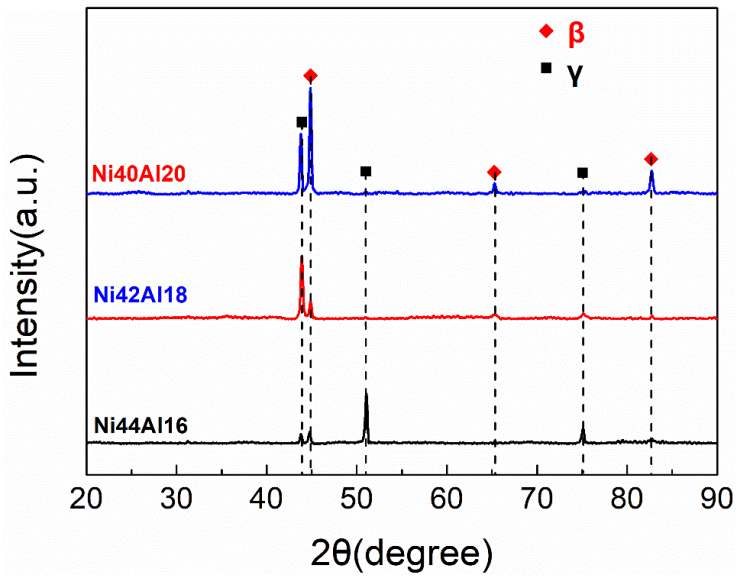


Fig. 2 XRD patterns of Ni44Al16, Ni42Al18 and Ni40Al20

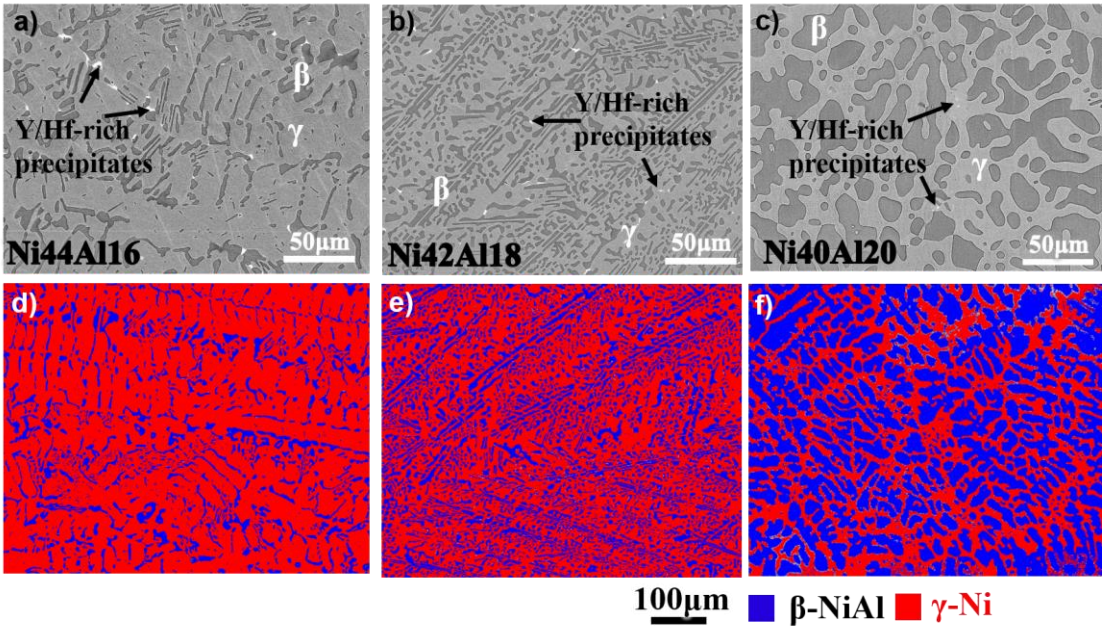


Fig. 3 Microstructural analysis of a, d) Ni44Al16, b,e) Ni42Al18 and c, f) Ni40Al20. For each column, the top is a BSE image (black arrows indicates the distribution of Y/Hf-rich precipitates) and the bottom is an EBSD phase map.

3.2 Microstructures of oxide scales

**Fig. 4** shows the surface morphology of the three alloys after 500 h oxidation at 1100 ℃. For all the alloys, the oxide morphologies show the uniform and dense α-$Al_2O_3$ scale with the uniformly distributed REs-oxide in the grain boundaries of α-$Al_2O_3$, which is well adherent to the alloy substrates. In addition, the oxide scales on the γ and β phases show different surface morphology, which might be attributed to the compositional difference between the two phases. **Fig. 5** presents the cross-sectional morphology and elemental distribution of the three alloys after 500 h oxidation at 1100 ℃. The $Al_2O_3$ scales formed on the three alloys are uniform and continuous and no interface imperfections (e.g., pores or oxide intrusions) are found at the scale/alloy interfaces. The amount and size of REs oxides (white contrast in **Fig. 5**) decrease with increase of Al content, which is well consistent with the distribution of Y/Hf precipitates (**Fig. 3a-c**). The thickness of oxide scale on Ni44Al16, Ni42Al18 and Ni40Al20 is ~4.5 μm, ~3.5 μm and ~2.7 μm, respectively. The finding suggests the oxidation rates of $Ni_{60-x}Co_{20}Cr_{20}Al_xYHf$ alloys can be lowered by increasing their Al content.

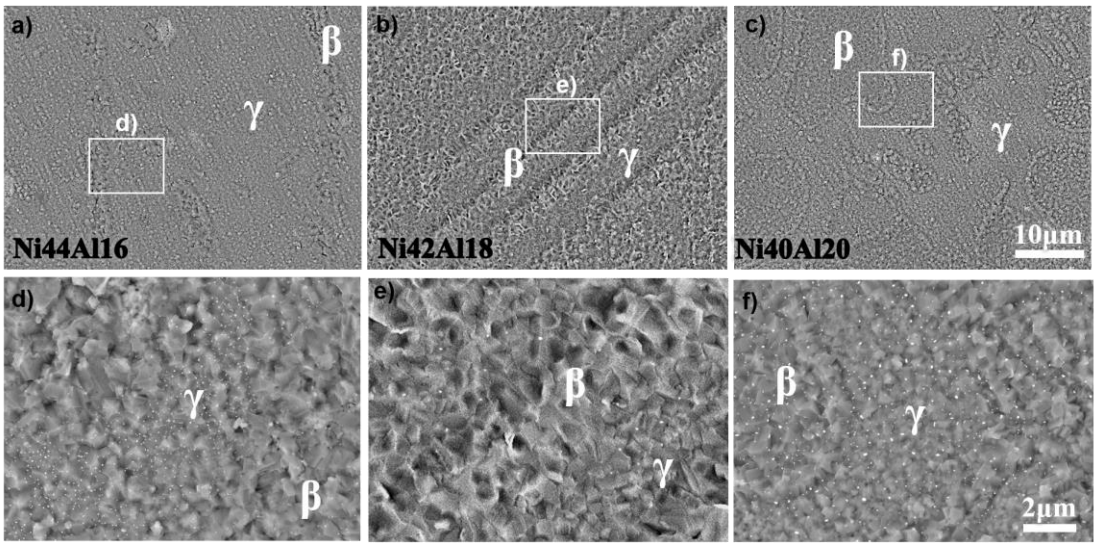


Fig. 4 Surface morphology of a, d) Ni44Al16, b, e) Ni42Al18 and c,f) Ni40Al20 after 500 h oxidation at 1100 ℃. The micrographs in the top a, b and c) and bottom d, e and f) rows are low and high magnification BSE images, respectively.

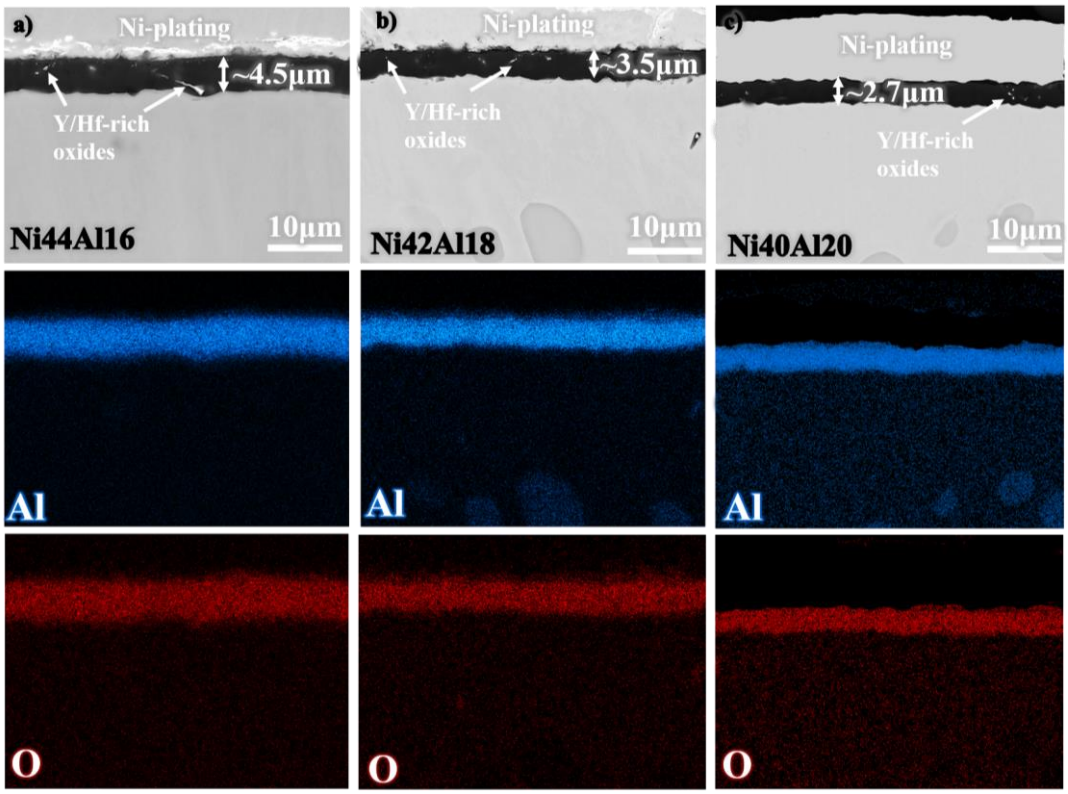


Fig. 5 Cross-sectional morphology and elemental distribution of (a) Ni44Al16, (b) Ni42Al18 and (c) Ni40Al20 after 500 h oxidation at 1100 ℃.

**Fig. 6a-c** shows the fractured cross-sectional microstructures of oxide scales formed on the three alloys after 500 h oxidation at 1100 ℃. The oxide scales show typical double-layer structure consisting of outer equiaxed grains and inner columnar grains. Compared to the inner columnar zones, the outer equiaxed zones are much thinner (400-500 nm) and their thickness is almost independent of the Al content. The predominant columnar grain structure suggests inward O diffusion dominated the oxide growth on the three alloys [38]. Quantitative image analysis of the oxide grain imprints **(Fig. 6d-i)** left on the three alloys shows the average width of columnar grains only increases slightly (from ~0.6μm to ~0.8μm) with the increase of Al content.

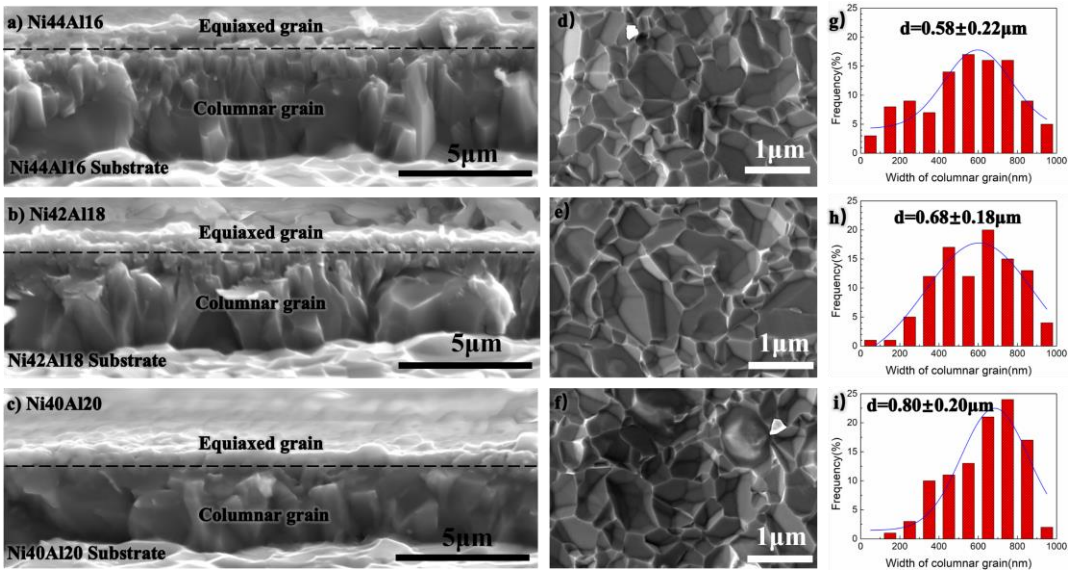


Fig. 6 Microstructural analysis of the oxide scales on a, d, g) Ni44Al16, b, e, h) Ni42Al18 and c, f, i) Ni40Al20 after 500 h oxidation at 1100 °C. The micrographs in the left column a-c) are fractured cross-sectional microstructures of the oxide scales (the black dash lines delineate the boundaries between the equiaxed grains and columnar grains). The micrographs in the middle column d-f) show the imprints left on the substrates by the columnar α-$Al_2O_3$ grains. The plots in the right column g-i) show the distribution of widths of columnar grains quantified from their imprints (based on at least 50 grains for each alloy). The fractured cross-sectional microstructures of the oxide scales are obtained by mechanical fracture test.

### 3.3 Oxidation kinetics

**Fig. 7** shows the evolution of oxide scale thickness with increasing oxidation time and the linear fitting of oxide scale thickness to the square root of oxidation time. The fitting to the square root of oxidation time is a straight line, which means oxidation of the three alloys obeys the parabolic law [39]. The parabolic rate constant $k_h$ is related to the scale thickness ($h_t$) and oxidation time $t$ by:

$$h_t^2 = k_h t \quad (1)$$

The parabolic rate constant $k_h$ can be converted into $k_p$ by [40]

$$k_p = \left(\frac{3M_O\rho_{Al_2O_3}}{M_{Al_2O_3}}\right)^2 k_h \quad (2)$$

Where $M_{Al_2O_3}$ and $M_O$ are the molar mass of $Al_2O_3$ and O; the $\rho_{Al_2O_3}$ is the density of $Al_2O_3$. The estimited parabolic rate constants $k_p$ are about $6.31 \times 10^{-13}$ $g^2$ $cm^4$ $s^{-1}$, $4.59 \times 10^{-13}$ $g^2$ $cm^4$ $s^{-1}$ and $2.61 \times 10^{-13}$ $g^2$ $cm^4$ $s^{-1}$ for Ni44Al16, Ni42Al18 and Ni40Al20, respectively. The results indicate $k_p$ has a positive correaltion with the Al content. Compared with the Ni44Al16 alloy, the Ni42Al18 alloy and Ni40Al20 alloy show a decrease of ~27% and ~58%, repectively, in $k_p$. The dependence of $k_p$ of $Ni_{60-x}Co_{20}Cr_{20}Al_x$ alloys on the Al content is in agreement with the work by Salam et al [41] on CoNiCrAlYRe coatings and Lu et al [42] on YHf co-doped NiFeCoCrAl alloys. These findings together suggest the Al content plays an important role in oxidation of MCrAlY coatings/alloys.

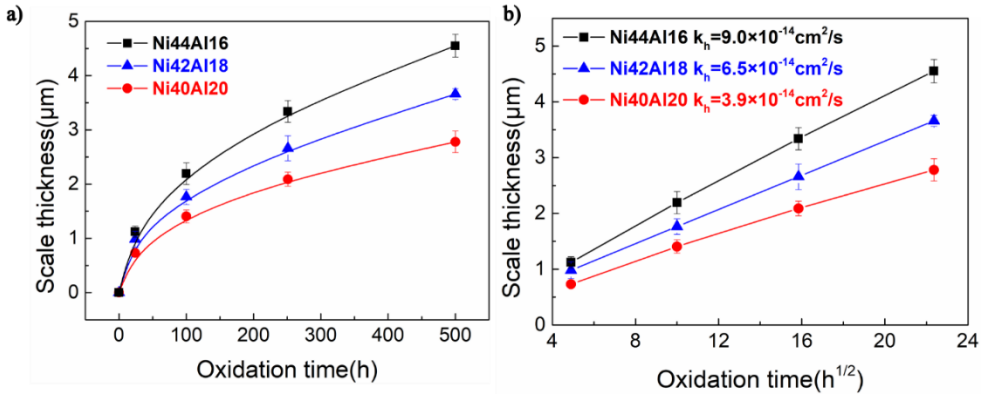


Fig. 7 Oxidation kinetics of the YHf co-doped NiCoCrAl alloys : a) thickness of the oxide scales as a function of oxidation time; b) thickness of the oxide scales on as a function of the square root of oxidation time, showing the parabolic law.

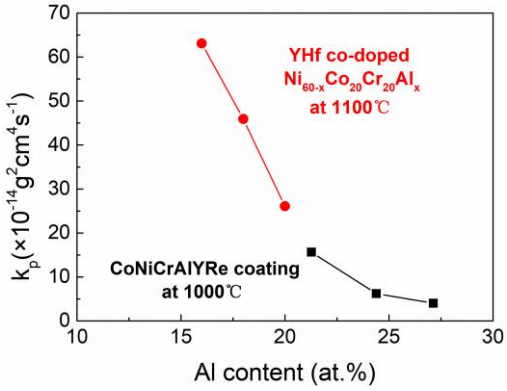


Fig. 8 The relationship between the parabolic rate constant $k_p$ and Al content (the data of CoNiCrAlYRe coatings are from the reference [41])

## 4. Discussion

It is well demonstrated in this work that the oxidation rates of NiCoCrAlYHf alloys can be lowered through increasing the Al content (**Fig. 5** and **Fig. 7**). A mechanistic understanding on this finding is of necessity for designing oxidation resistant alloys or coatings. Therefore, the following section will devote to discuss the effect of Al content on the oxidation behavior of NiCoCrAlYHf alloys.

### *4.1 Maintenance of exclusive $Al_2O_3$ formation at 1100 ℃*

The uniform and continuous $Al_2O_3$ scale develops on three alloys after 500 h oxidation at 1100 ℃ and this result shows that the Al concentration is sufficient to maintain the growth of $Al_2O_3$ scale during the long-term oxidation (**Fig. 5**). Once the continuous $Al_2O_3$ scale is formed, the minimum Al concentration required to maintain the growth of exclusive $Al_2O_3$ and formation of other transient oxides should be determined. All alloys are two-phase structure of γ and β phases (**Fig. 3**). The Al-rich β phase can favor the formation of exclusive $Al_2O_3$ scale, and thus the maintenance for the exclusive $Al_2O_3$ scale is determined the Al-poor γ phase (**Table. 2**). It is necessary to ascertain the effect of Al content on the minimum Al concentration of γ phase in three alloys to develop the $Al_2O_3$ scale. According to the Wagner theory, the minimum Al concentration required to maintain exclusive $Al_2O_3$ formation can be expressed as following [43]:

$$N_{Al(min)}^{\gamma}=\left(\frac{\pi g^{*} N_O^{\gamma} D_O^{\gamma} V_m^{\gamma}}{2bD_{Al}^{\gamma} V_m^{Al_2O_3}}\right)^{1/2} \quad (3)$$

where the $N_{Al(min)}^{\gamma}$ is the minimum Al concentration for the γ-Ni to develop the external $Al_2O_3$ scale; b is the coefficient of the oxide in $MO_b$ type, e.g., $AlO_{3/2}$;$D_{Al}^{\gamma}$ is the diffusion coefficient of Al in γ-Ni; $V_m^{Al_2O_3}$and $V_m^{\gamma}$ is the molar volume of the $Al_2O_3$ and γ-Ni, respectively; $g^{*}$ is the critical volume fraction of $Al_2O_3$, which is usually taken as 0.1-0.7; $N_O^{\gamma}$ is solubility of oxygen in the γ-Ni; $D_O^{\gamma}$ is the diffusion coefficient of oxygen in the γ-Ni; $N_O^{\gamma}D_O^{\gamma}$ is the oxygen permeability in γ -Ni. The

calculation of $N_{Al(min)}^{\gamma}$ need the value of $N_O^{\gamma}D_O^{\gamma}$ and $D_{Al}^{\gamma}$, which are unknown in the **Eq. (3)**. The $D_{Al}^{\gamma}$ can be obtained by the DICTRA module of thermo-calc software (**Table. 3**). Additionally, the value of $N_O^{\gamma}D_O^{\gamma}$ can be retrieved from the oxidation kinetics and classic oxidation theory [44]:

$$h_t = \left(\frac{2N_O^{\gamma}D_O^{\gamma}}{bN_{Al}^0}t\right)^{1/2} \quad (4)$$

$$h_t = (k_p t)^{1/2} \quad (5)$$

where the $h_t$ is the $Al_2O_3$ thickness, t is the oxidation time and $N_{Al}^0$ is the initial concentration of Al in the γ-Ni. $k_p$ is the parabolic oxidation rate, which is gained by fitting the experimental results (**Fig. 7**). The value of $N_O^{\gamma}D_O^{\gamma}$ can be estimated by the **Eq. (4)** [44] and **Eq. (5)**. The critical volume fraction of $Al_2O_3$ $g^*$ may be difficult to obtain due to the microstructural difference of three alloys. However, it can be evaluated by setting some specific values for $g^*$ according to the published reference, e,g. 0.1-0.7 [45-46]. Finally, the relationship between the $N_{Al(min)}^{\gamma}$ and $g^*$ was established, as shown in the **Fig. 9**. It can be found that the $N_{Al(min)}^{\gamma}$ decreases along the increasing Al content and is lower than 8 at.% for all alloys. In other words, the initial Al concentration (~12 at.%) in γ phase for three alloys (**Table. 2**) is much higher the calculated $N_{Al(min)}^{\gamma}$. Therefore, the effect of Al content on the exclusive $Al_2O_3$ growth for the NiCoCrAlYHf alloys in this study is negligible.

Table 3 the calculated Al diffusion coefficient of γ phase in each alloy at 1100℃ by the TC

| Alloys | Al diffusion coefficient of γ phase ($cm^2/s$) |
|---|---|
| Ni44 Al16 | $9.44\times10^{-14}$ |
| Ni42 Al18 | $9.56\times10^{-14}$ |
| Ni40 Al20 | $9.67\times10^{-14}$ |

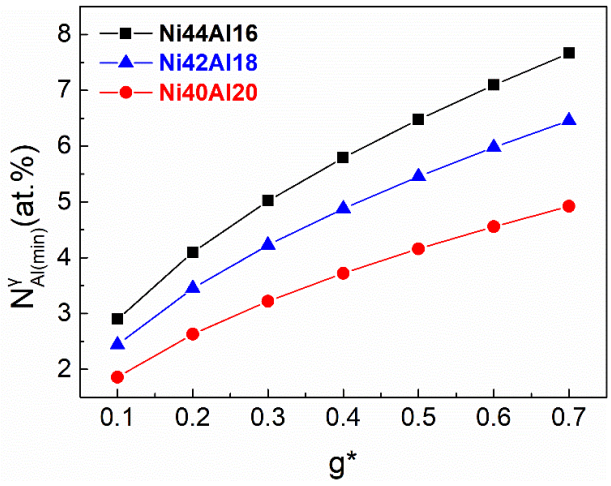


Fig. 9 Calculated the minimum Al concentration for the γ-Ni phase to develop the external $Al_2O_3$ scale $N^{\gamma}_{Al(min)}$ in Ni44Al16/ Ni42Al18/Ni40Al20 alloy at 1100℃

*4.2. Effect of width of columnar grain on the oxidation rate*

It is clearly seen in **Fig. 6** that the oxide scales formed on the three alloys are double-layer structure composed of outer equaixed grains and inner columnar grains. The thickness of equaixed zones and columnar zones as a function of oxidation time is shown in **Fig. 10**. The thickness of equaixed zones on all the three alloys is small (~500 nm) and shows little change with increasing oxidation time. Therefore, the apparent difference in scale thickness between the three alloys is governed by the growth of columnar grains (**Fig. 10b**). For RE-doped $Al_2O_3$-forming alloys, the growth of oxide scales is dominated by the inward O diffusion because of the dynamic segregation effect of RE [47]. Meanwhile, the thickness ratio ($h_{equiaxed\ grain}/h_{total}$) of all those alloy are lower

than 20% above 250 h oxidation (**Fig. 10c**), which also suggests the importance of O diffusion. An implication of this theory is that a larger $Al_2O_3$ grain size may result in a lower oxide growth rate because the $Al_2O_3$ grain boundaries are inward O diffusion paths. According to results in **Fig. 10d** and **Fig. 6**, the widths of columnar $Al_2O_3$ grains formed on the three alloys range from ~0.6 μm to ~0.8 μm with the increase of Al content. Compared with the Ni44Al16 alloy, the Ni42Al18 alloy and Ni40Al20 alloy show a increase of ~17% and ~34%, repectively. This suggests $Al_2O_3$ grain size is the important factor that gives rise to the difference in oxidation rates between the three alloys. The difference of columnar grain may be explained by the increase of volume fraction of β phase with increasing the Al content. It is reported that the β phase have larger probability to form the θ-$Al_2O_3$ than the γ phase [12,48]. The PLPS spectra was collected from the specimen after short time oxidation to confirm the phase constitution of θ-$Al_2O_3$, as shown in **Fig. 11a-c**. Based on the PLPS results and **Eq. (6)**, the content of θ-$Al_2O_3$ (wt.%) on Ni44Al16, Ni42Al18 and Ni40Al20 is calculated, yielding ~12%, ~8% and ~10%, respectively.

$$C_\theta = \frac{A_{14575}+A_{14645}}{A_{14402}+A_{14432}+A_{14575}+A_{14645}} \quad (6)$$

where A denotes the area of characteristic peaks (calculated by the deconvolution integration method), and the subscript represents the peak wavenumber. Hence, the content of θ-$Al_2O_3$ in the whole oxide scale can be roughly estimated by multiplying the calculated θ-$Al_2O_3$ content with the volume fraction of the β phase, as seen in **Table. 4**. Moreover, according to the SEM analysis (**Fig. 11d-i**), it can be observed that the θ-$Al_2O_3$ (needle-like morphology in the **Fig. 11g-i**) is mainly formed on the β phase. This means that the increase of volume fraction of β phase will lead to the more θ-$Al_2O_3$ at early oxidation stage. The decelerated θ- to α-$Al_2O_3$ phase transformation can decrease the number of sites for nucleation of α-$Al_2O_3$, which results in a larger $Al_2O_3$ grain [49]. For instance, the NiCrAl alloy has higher oxidation rate than NiAl alloy because the chromium accelerates the phase transformation, and thus formed the fine grained α-$Al_2O_3$ [50]. Eventually, the columnar grain size increases with the Al content can be attributed to its influence on the θ- to α-$Al_2O_3$ phase transformation rate. Nevertheless,

this inference need further work to confirm it.

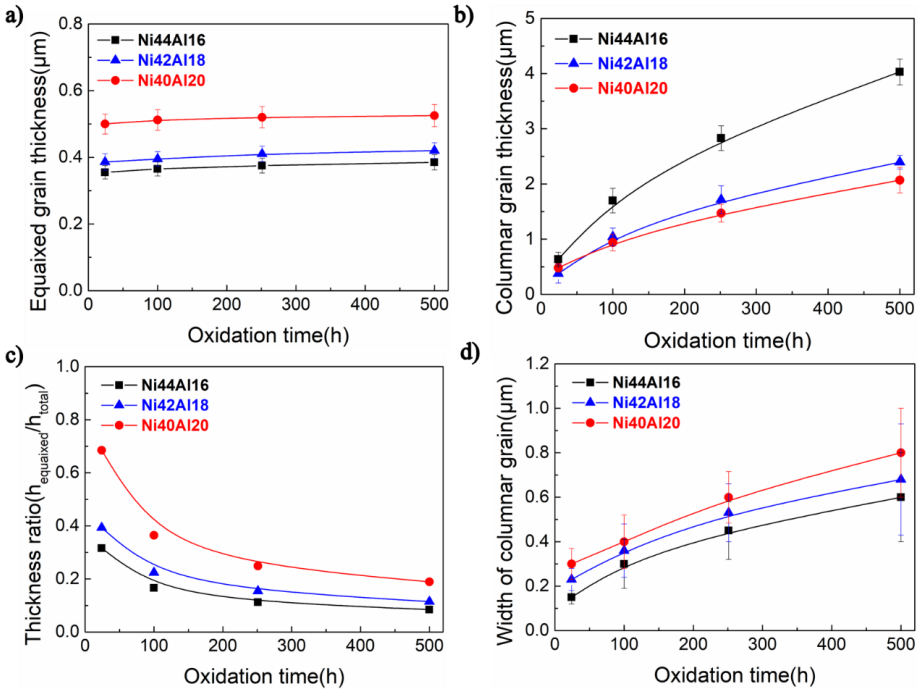


Fig. 10 Evolution of (a) equiaxed zone thickness, (b) columnar zone thickness, (c) thickness ratio ($h_{equiaxed\ grain}/h_{total}$) and (d) widths of columnar $Al_2O_3$ grains as a funciton of oxidation time of the YHf co-doped $Ni_{60-x}Co_{20}Cr_{20}Al_x$ alloys at 1100℃

Table 4 Calculated content of θ-$Al_2O_3$ in the whole oxide scale in each alloy after 5 min oxidation at 1100 ℃

| Alloy | θ-$Al_2O_3$ content in the whole oxide scale(wt.%) |
|---|---|
| Ni44Al16 | 2.1% |
| Ni42Al18 | 3.5% |
| Ni40Al20 | 6.4% |

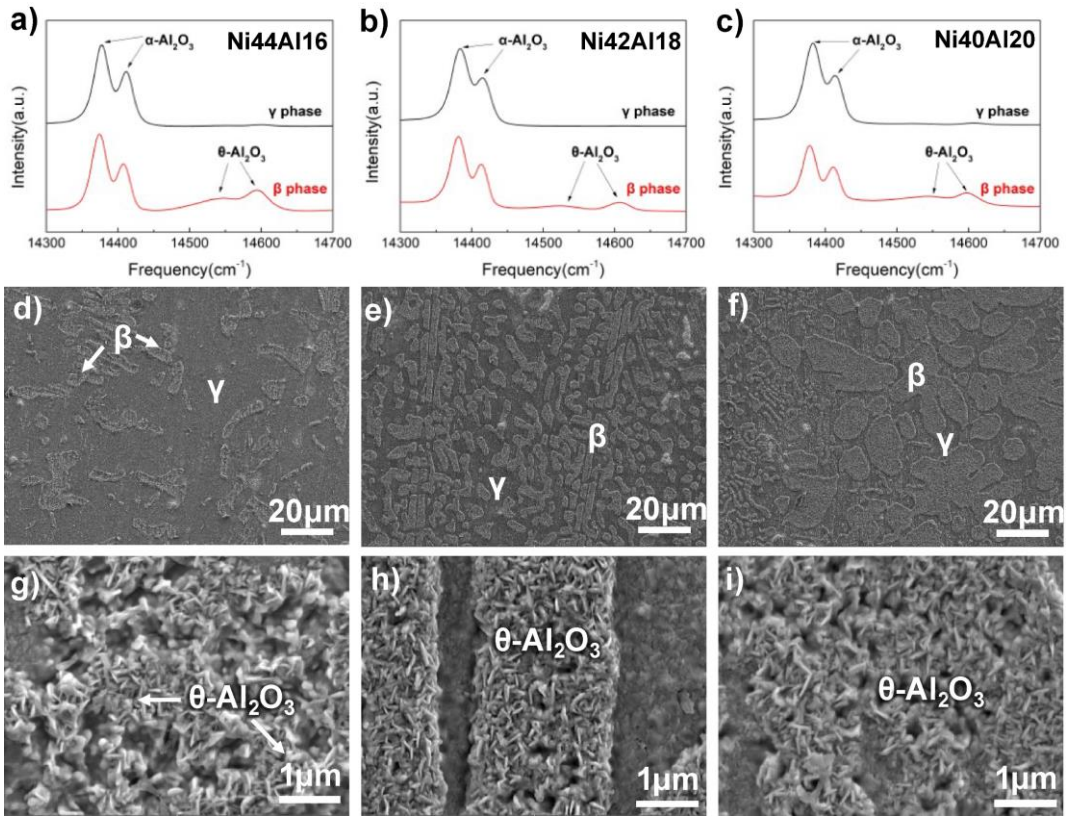


Fig. 11 PLPS spectra and microstructure analysis of $Al_2O_3$ scale formed on the (a, d, g) Ni44Al16, (b, e, h) Ni42Al18 and (c, f, i) Ni40Al20 after 5 min oxidation at 1100℃. The micrographs in the middle (d, e and f) are low magnification SE images, showing the overview of surface morphology. The bottom (g, h and i) rows are high magnification SE images, showing the surface morphology of θ-$Al_2O_3$ formed on the β phase.

### *4.3. Effect of RE-rich oxides incorporated into $Al_2O_3$ scale on the oxidation rate*

Although the higher grain size of columnar grain could cause the decrease of oxidation rate, it cannot compose the full story as its difference is smaller than that in oxidation rates. The effect of Al diffusion and REs-rich oxides may be other important factors on the oxidation rates. For studying the contribution of Al diffusion, the Al diffusion coefficient and activity of fcc-structured Al-depleted layer at 1100 ℃ (**Table. 6**) are calculated by TC. The composition of Al-depleted layer is obtained from SEM-EDS point analysis, as shown in **Table. 5**. Although the Al diffusion coefficient and activity increases as the the Al content increases, there are no distinct difference between those

three alloys. This means the Al diffusion have limited influence on the oxidation rate.

Table 5 Chemical compositions (at.%) of Al-depleted layer in each alloy after 500h oxidation at 1100℃.(The chemical composition is the average value taken from EDS analysis in five different points)

| Elements | Ni44Al16 | Ni42Al18 | Ni40Al20 |
|---|---|---|---|
| Ni | 42.0±1.4 | 37.2±1.5 | 34.9±1.6 |
| Co | 22.1±1.3 | 24.1±1.4 | 25.6±1.2 |
| Cr | 23.3±1.5 | 27.2±1.6 | 28.8±1.5 |
| Al | 12.6±1.2 | 11.5±1.1 | 10.7±0.9 |

Table 6 Calculated Al diffusion coefficient of Al-depleted layer in each alloy at 1100℃ by the TC

| Alloy | $D_{Al}$(cm$^2$/s) |
|---|---|
| Ni44Al16 | $1.39\times10^{-13}$ |
| Ni42Al18 | $1.53\times10^{-13}$ |
| Ni40Al20 | $1.60\times10^{-13}$ |

It is well accepted that the O diffusion coefficient at α-$Al_2O_3$ scale was higher several order magnitude than Al diffusion coefficient in RE-doped alloy according to reported literatures [51-52]. Thus, the inward oxygen diffusion is the key factor to control the oxidation kinetics. Except the width of columnar grain, the amount and size of RE-rich oxides within the $Al_2O_3$ scale are important for the O diffusion rate because of its much faster O diffusivity than that in the $Al_2O_3$ [22,53-54]. The Y/Hf-rich precipitates can act important role on the distribution of REs-rich oxides within the $Al_2O_3$ scale. For understanding the the effct of Al content on the distribution of Y/Hf-rich precipitates, the Y/Hf solubility of γ and β phase in each alloys are calculated by the TC, as shown

in **Fig. 12** and **Table. 7**. It can be seen that the Y/Hf solubility of β phase is much higher (about ×4) than γ phase in all the alloys. Therefore, as the volume fraction of β phase fraction increase with the increase of Al content, the Y/Hf-rich precipitates present the decrease trend (**Fig. 3a-c**). Meanwhile, followed by the SEM-analysis of **Fig. 5a-c**, the amount and size of RE-rich oxides within the $Al_2O_3$ scale is also decreased with the increase of Al content. The TEM analysis for oxidation scale of Ni44Al16 and Ni40Al20 after 500h oxidation at 1100℃ is presented in **Fig. 13** to deeply analyse the distribution of REs-rich oxides within $Al_2O_3$ scale. It can be seen that the amount and size of REs-rich oxides of Ni44Al16 (~300 nm) is much larger than that in Ni40Al20 (~50 nm). Those larger REs-rich oxides can be regarded as the short-circuit path for O diffusion, which can accelerate the O diffusion rate. As the Al content increases, the size and amount of REs-rich oxides decrease with the increase of volume fraction of β phase, which can reduce the short-circuit paths for O diffusion. Therefore, the O diffusion rate decreases with increasing the Al content. Eventually, the Al content plays an important role on the O diffusion rate by its important influence on the distribution of REs-rich oxides within $Al_2O_3$ scale.

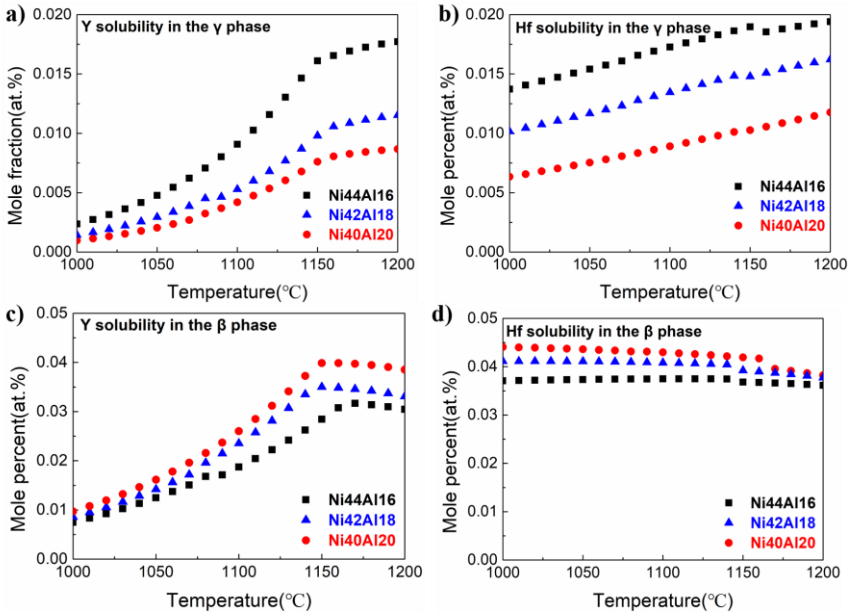


Fig. 12 Calculated Y/Hf solubility of γ and β phase in $Ni_{60-x}Co_{20}Cr_{20}Al_x$ alloys at 1000-1200℃: a) Y solubility and b) Hf solubility in the γ phase; c) Y solubility and d) Hf solubility in the β phase.

Table 7 Calculated Y and Hf solubility (at.%) of β and γ in each alloy at 1100℃.

| Alloy | Y solubility in γ phase | Y solubility in β phase | Hf solubility in γ phase | Hf solubility in β phase |
|---|---|---|---|---|
| Ni44 Al16 | 0.009 | 0.019 | 0.017 | 0.037 |
| Ni42 Al18 | 0.005 | 0.023 | 0.013 | 0.041 |
| Ni40 Al20 | 0.004 | 0.031 | 0.010 | 0.043 |

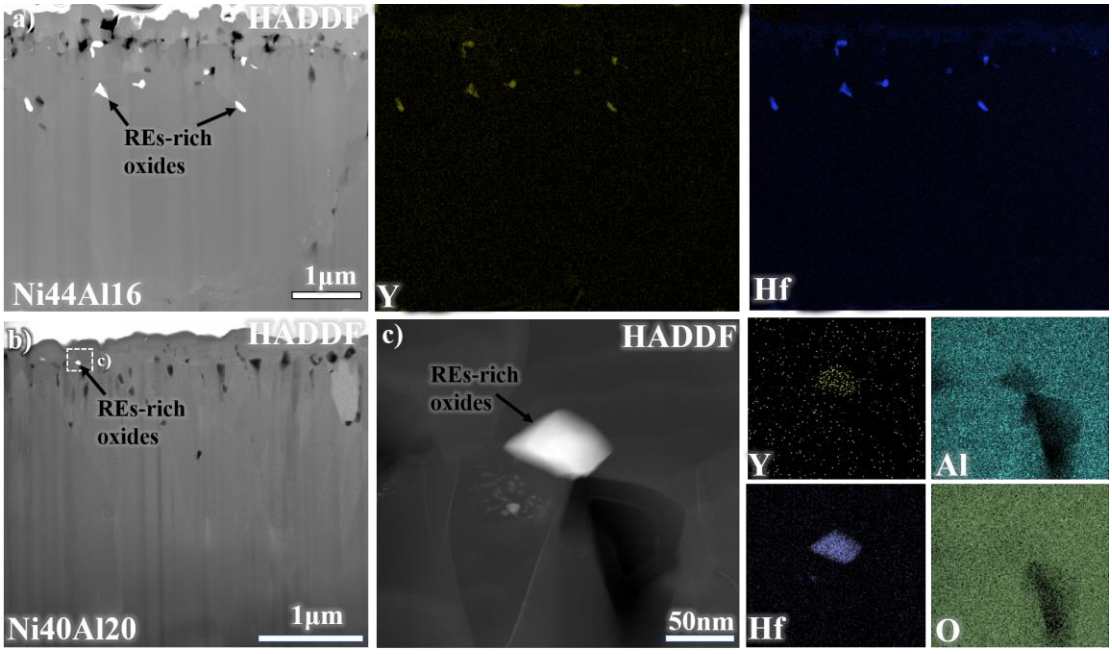


Fig. 13 STEM-EDS analysis of oxide scale after 500h oxidation at 1100℃, showing the distribution of Y/Hf-rich oxides: a) STEM-HAADF image combined with EDS mapping of Ni44Al16 and b) STEM-HAADF image of Ni40Al20 and c) the enlarged HADDF image combined with EDS mapping from the white shadow from b).

## 5. Conclusions

In this work, the YHf co-doped $Ni_{60-x}Co_{20}Cr_{20}Al_x$ (x=16, 18 and 20 at.%) alloy with varying Al contents were designed using CALPHAD, to understand the effect of Al content on the scale growth mechanism under isothermal oxidation at 1100℃. Based on our findings and analysis, we can draw the following conclusions:

1. The oxidation rate decreases with the increase of Al content. This suggests that a higher Al content contributes to improved oxidation resistance.

2. The columnar grain size increases with the increase of Al content, which can decrease the oxidation rate due to the reduction of O diffusion path. The content of $\theta$-$Al_2O_3$ increases with increasing the Al content at initial oxidation stage, which could result in larger columnar grain size.

3. The amount and size of REs-rich oxides within $Al_2O_3$ scale decrease with increasing the Al content, which is also responsible for the reduction of oxidation rate due to the reduction of short-circuit paths for O diffusion. This is attributed to the much higher Y/Hf solubility in $\beta$ phase than in $\gamma$ phase.

Above all, the Al content is critical for the oxidation rate of Y/Hf co-doped NiCoCrAl alloy due to its vital role on the O diffusion rate.

## Acknowledgements

This work was supported by National Natural Science Foundation of China (No. 52201082, No.52102072 and No. 51971139) and Shanghai Sailing Program (No. 22YF1419200). This work is also sponsored by Chenguang Program supported by Shanghai Education Development Foundation and Shanghai Municipal Education Commission (No. 21CGA10).

## References


[1] D. Naumenko, B.A. Pint, W.J. Quadakkers, Current Thoughts on Reactive Element Effects in Alumina-Forming Systems: In Memory of John Stringer, Oxid. Met. 86 (2016) 1–43.

[2] C.G. Levi, Emerging materials and processes for thermal barrier systems, Current Opinion in Solid State and Materials Science 8(1) (2004) 77–91.

[3] Y. Chen, X. Zhao, Y. Dang, P. Xiao, N. Curry, N. Markocsan, P. Nylen, Characterization and understanding of residual stresses in a NiCoCrAlY bond coat for thermal barrier coating application, Acta Mater. 94 (2015) 1–14.

[4] N.P. Padture, M. Gell, E.H. Jordan, Thermal barrier coatings for gas-turbine engine applications, Science (80). 296 (2002) 280–284.

[5] C.S. Giggins, F.S. Pettit, Oxidation of Ni-Cr-Al Alloys Between 1000 and 1200°C, J. Electrochem. Soc. 118 (1971) 1782.

[6] G.R. Wallwork, The oxidation of alloys, Reports Prog. Phys. 39 (1976) 481–485.

[7] C.A. Barrett, C.E. Lowell, Resistance of Ni-Cr-Al alloys to cyclic oxidation at 1100 and 1200°C, Oxid. Met. 11 (1977) 199–223.

[8] J.W. Hutchinson, M.Y. He, A.G. Evans, Influence of imperfections on the nucleation and propagation of buckling driven delaminations, J. Mech. Phys. Solids. 48 (2000) 709–734.

[9] E.P. Busso, L. Wright, H.E. Evans, L.N. McCartney, S.R.J. Saunders, S. Osgerby, J. Nunn, A physics-based life prediction methodology for thermal barrier coating systems, Acta Mater. 55 (2007) 1491–1503.

[10] F. Cao, B. Tryon, C.J. Torbet, T.M. Pollock, Microstructural evolution and failure characteristics of a NiCoCrAlY bond coat in “hot spot” cyclic oxidation, Acta Mater. 57 (2009) 3885–3894.

[11] Z. Zhao, J. Wang, M. Chen, J. Zhang, F. Wang, D.J. Young, Comparative study on the initial oxidation behavior of conventional and nanocrystalline MCrAlY coatings- effect of microstructure evolution and dynamic mechanisms, Acta Mater. 239 (2022) 118264.

[12] Y. Chen, X. Zhao, P. Xiao, Effect of microstructure on early oxidation of MCrAlY coatings, Acta Mater. 159 (2018) 150–162.

[13] Y. Yang, H. Yao, Z. Bao, P. Ren, W. Li, Modification of NiCoCrAlY with Pt: Part I. Effect of Pt depositing location and cyclic oxidation performance, J. Mater. Sci. Technol. 35 (2019) 341–349.

[14] C. Yu, H. Liu, C. Jiang, Z. Bao, S. Zhu, F. Wang, Modification of NiCoCrAlY with Pt: Part II. Application in TBC with pure metastable tetragonal (t ’) phase YSZ and thermal cycling behavior, J. Mater. Sci. Technol. 35 (2019) 350–359.

[15] J. Lu, Y. Chen, C. Zhao, H. Zhang, L. Luo, B. Xu, X. Zhao, F. Guo, P. Xiao, Significantly improving the oxidation and spallation resistance of a MCrAlY alloy by controlling the distribution of yttrium, Corros. Sci. 153 (2019) 178–190.

[16] J. Lu, Y. Chen, H. Zhang, C. Zhao, X. Zhao, F. Guo, P. Xiao, Superior oxidation and spallation resistant NiCoCrAlY bond coat via homogenizing the yttrium distribution, Corros. Sci. 159 (2019) 108145.

[17] A.H. Heuer, D.B. Hovis, J.L. Smialek, B. Gleeson, Alumina Scale Formation: A New Perspective, J. Am. Ceram. Soc. 94 (2011) s146–s153.

[18] A.H. Heuer, T. Nakagawa, M.Z. Azar, D.B. Hovis, J.L. Smialek, B. Gleeson, N.D.M. Hine, H. Guhl, H.-S. Lee, P. Tangney, W.M.C. Foulkes, M.W. Finnis, On the growth of $Al_2O_3$ scales, Acta Mater. 61 (2013) 6670–6683.

[19] D. Naumenko, B. Gleeson, E. Wessel, L. Singheiser, W.J. Quadakkers, Correlation between the microstructure, growth mechanism, and growth kinetics of alumina scales on a FeCrAlY alloy, Metall. Mater. Trans. A Phys. Metall. Mater. Sci. 38 A (2007) 2974–2983.
[20] J.L. Smialek, N.S. Jacobson, B. Gleeson, D.B. Hovis, A.H. Heuer, Oxygen Permeability and Grain-Boundary Diffusion Applied to Alumina Scales, Nasa Tm 217855. (2013) 1–14.
[21] T.J. Nijdam, W.G. Sloof, Effect of reactive element oxide inclusions on the growth kinetics of protective oxide scales, Acta Mater. 55 (2007) 5980–5987.
[22] J. Lu, Y. Chen, H. Zhang, L. He, R. Mu, Z. Shen, X. Zhao, F. Guo, Y/Hf-doped $Al_{0.7}$CoCrFeNi high-entropy alloy with ultra oxidation and spallation resistance at 1200 ℃, Corros. Sci. 174 (2020) 108803.
[23] J.C. Pereira, J.C. Zambrano, E. Rayon, A. Yanez, V. Amigo, Mechanical and microstructural characterization of MCrAlY coatings produced by laser cladding: The influence of the Ni, Co and Al content, Surf. Coat. Technol. 338 (2018) 22–31.
[24] Y. Li, C. Li, Q. Zhang, L. Xing, G. Yang, Effect of Chemical Compositions and Surface Morphologies of MCrAlY Coating on Its Isothermal Oxidation Behavior, J. Therm. SPRAY Technol. 20 (2011) 121–131.
[25] H. Chen, L. Li, R. Yang, W. Zhu, A. Rushworth, Y. Yin, X. Wang, Microstructure and thermophysical properties of as-cast CoNiCrAl bond coat alloys at different Al contents, J. Alloys Compd. 918 (2022) 165575.
[26] H. Chen, T. Barman, Thermo-Calc and DICTRA modelling of the beta-phase depletion behaviour in CoNiCrAlY coating alloys at different Al contents, Comput. Mater. Sci. 147 (2018) 103–114.
[27] W. Kai, Z. Jiang, G. Chen, I. Lee, H. Lin, H.H. Hsieh, W. Lin, J. Kai, High-temperature air-oxidation of $NiCoCrAl_x$ medium-entropy alloys, Corros. Sci. 192 (2021) 109858.
[28] A. Takeuchi, A. Inoue, Classification of Bulk Metallic Glasses by Atomic Size Difference, Heat of Mixing and Period of Constituent Elements and Its Application to Characterization of the Main Alloying Element, Mater. Trans. 46 (2005) 2817–2829.
[29] T.J. Nijdam, W.G. Sloof, Effect of Y distribution on the oxidation kinetics of NiCoCrAlY bond coat alloys, Oxid. Met. 69 (2008) 1–12.
[30] D. Naumenko, B.A. Pint, W.J. Quadakkers, Current Thoughts on Reactive Element Effects in Alumina-Forming Systems: In Memory of John Stringer, Oxid. Met. 86 (2016) 1–43.
[31] B.A. Pint, Optimization of reactive-element additions to improve oxidation performance of alumina-forming alloys, J. Am. Ceram. Soc. 86 (2003) 686–95.
[32] J.-O. Andersson, T. Helander, L. Höglund, P. Shi, B. Sundman, Thermo-Calc & DICTRA, computational tools for materials science, Calphad 26(2) (2002) 273–312.
[33] X. Liu, G. Lindwall, T. Gheno, Z. Liu, Thermodynamic modeling of Al–Co–Cr, Al–Co–Ni, Co–Cr–Ni ternary systems towards a description for Al–Co–Cr–Ni, Calphad. 52 (2016) 125–142.
[34] M.J. Pomeroy, Coatings for gas turbine materials and long term stability issues, Mater. Des. 26 (2005) 223–231.
[35] G.W. Goward, Progress in coatings for gas turbine airfoils, Surf. Coat. Technol. 108 (1998) 73–79.
[36] R.C. Reed, The superalloys: fundamentals and applications, Cambridge university press2008.
[37] X. Liu, Y. Chen, J. Lu, L. Li, A. Huang, H. Zhang, X. Fan, X. Zhang, X. Zhao, A comparative study on the oxidation behavior of Y-, Hf- and YHf-doped NiCoCrAl alloys: Effect of reactive

elements, Corros. Sci. 218 (2023) 111160.
[38] B.A. Pint, J.R. Martin, L.W. Hobbs, 18O/SIMS characterization of the growth mechanism of doped and undoped α-$Al_2O_3$, Oxid. Met. 39(3) (1993) 167–195.
[39] D.J. Young, High temperature oxidation and corrosion of metals, Elsevier2008.
[40] J. Lu, H. Zhang, Y. Chen, L. Ling, X. Liu, W. Xiao, N. Ni, X. Zhao, F. Guo, P. Xiao, Y-doped $AlCoCrFeNi_{2.1}$ eutectic high-entropy alloy with excellent oxidation resistance and structure stability at 1000 ℃ and 1100 ℃, Corros. Sci. 180 (2021) 109191.
[41] S. Salam, P. Hou, Y. Zhang, H. Wang, C. Zhang, Z. Yang, Compositional effects on the high-temperature oxidation lifetime of MCrAlY type coating alloys, Corros. Sci. 95 (2015) 143–151.
[42] J. Lu, Y. Chen, H. Zhang, L. Li, L. Fu, X. Zhao, F. Guo, P. Xiao, Effect of Al content on the oxidation behavior of Y/Hf-doped AlCoCrFeNi high-entropy alloy, Corros. Sci. 170 (2020) 108691.
[43] N. Birks, G.H. Meier, F.S. Pettit, Introduction to the high temperature oxidation of metals, Cambridge university press2006.
[44] Y. Wu, Y. Li, Y. Xu, M. Kang, J. Wang, B. Sun, Unveiling the mechanism of yttrium-related microstructure inhibiting or promoting high-temperature oxidation based on Ni-Al-Y alloys, Acta Mater. 211 (2021) 116879.
[45] Z. Zhang, F. Gesmundo, P. Hou, Y. Niu, Criteria for the formation of protective $Al_2O_3$ scales on Fe–Al and Fe–Cr–Al alloys, Corros. Sci.48(3) (2006) 741–765.
[46] R.A. Rapp, Kinetics, microstructures and mechanism of internal oxidation-its effect and prevention in high temperature alloy oxidation, Corrosion 21(12) (1965) 382–401.
[47] B.A. Pint, Experimental observations in support of the dynamic-segregation theory to explain the reactive-element effect, Oxid. Met. 45 (1996) 1–37.
[48] C.G. Levi, E. Sommer, S.G. Terry, A. Catanoiu, M. Rühle, Alumina grown during deposition of thermal barrier coatings on NiCrAlY, J. Am. Ceram. Soc. 86 (2003) 676–685.
[49] M.W. Brumm, H.J. Grabke, The oxidation behaviour of NiAl-I. Phase transformations in the alumina scale during oxidation of NiAl and NiAl-Cr alloys, Corros. Sci. 33 (1992) 1677–1690.
[50] B.A. Pint, K.L. More, I.G. Wright, Effect of quaternary additions on the oxidation behavior of Hf-doped NiAl, Oxid. Met. 59 (2003) 257–283.
[51] T. Boll, V. Babic, I. Panas, O. Bäcke, K. Stiller, On aliovalent cations control of α-alumina growth on doped and undoped NiAl, Acta Mater. 210 (2021) 116809.
[52] K.P.R. Reddy, J.L. Smialek, A.R. Cooper, 18O Tracer studies of $Al_2O_3$ scale formation on NiCrAl alloys, Oxid. Met. 17 (1982) 429–449.
[53] A. Gil, D. Naumenko, R. Vassen, J. Toscano, M. Subanovic, L. Singheiser, W.J. Quadakkers, Y-rich oxide distribution in plasma sprayed MCrAlY-coatings studied by SEM with a cathodoluminescence detector and Raman spectroscopy, Surf. Coat. Technol. 204 (2009) 531–538.
[54] H. Peng, H. Guo, J. He, S. Gong, Cyclic oxidation and diffusion barrier behaviors of oxides dispersed NiCoCrAlY coatings, J. Alloys Compd. 502 (2010) 411–416.